

Near 100% CO Selectivity in Nanoscaled Iron-Based Oxygen Carriers for Chemical Looping Methane Partial Oxidation

Yan LIU^{a†}, Lang QIN^{a†}, Zhuo CHENG^{a†}, Josh W. GOETZE^a, Fanhe KONG^a, Jonathan A. FAN^b, Liang-Shih FAN^{a*}

^a Department of Chemical and Biomolecular Engineering, the Ohio State University, 151 W Woodruff Ave, Columbus, OH 43210, USA.

^b Department of Electrical Engineering, Ginzton Laboratory, Spilker Engineering and Applied Sciences, 348 Via Pueblo Mall, Stanford University, Stanford, CA 94305, USA.

[†] Co-first authors

* Corresponding Author, fan.1@osu.edu

Abstract

Chemical looping methane partial oxidation provides an energy and cost effective route for methane utilization. However, there is considerable CO₂ co-production in state-of-the-art chemical looping systems, rendering a decreased productivity in value-added fuels or chemicals. In this work, we show that the co-production of CO₂ can be dramatically suppressed in methane partial oxidation reactions using iron oxide nanoparticles, with a size of 5±3 nm, as the oxygen carrier. To stabilize these nanoparticles at high temperatures, they are embedded in an ordered, gas-permeable mesoporous silica matrix. We experimentally obtained near 100% CO selectivity in a cyclic redox system at 750 °C to 935 °C, which is a significantly lower temperature range than in conventional oxygen carrier systems. Density functional theory calculations elucidate the origins for such selectivity and reveal that CH₄ adsorption energies decrease with increasing nanoparticle size. These calculations also show that low-coordinated lattice oxygen atoms on the surface of nanoparticles significantly promote Fe-O bond cleavage and CO formation. We

envision that embedded nanostructured oxygen carriers have the potential to serve as a general materials platform for achieving 100% selectivity in redox reactions at high temperatures.

Syngas, i.e., CO and H₂, is an important intermediate for producing fuels and value-added chemicals from methane via Fischer-Tropsch or other synthesis techniques¹. Syngas has been produced commercially by steam reforming, auto-thermal reforming, and partial oxidation of methane for many decades². However, an improvement of its energy consumption, environmental impact, and associated production cost has always been of interest. This has prompted the investigation into alternative routes that can avoid the use of air separation units for producing purified oxygen and are more effective in CO₂ emission control. It is also of interest to reduce the operating temperature of these processes, which are generally endothermic and traditionally require temperatures of 900 °C or higher to attain high reactant conversion rates. The use of high temperatures is problematic because the thermodynamic driving force for carbon deposition, and thus materials obliteration, can be accelerated³. Current approaches to reducing reaction temperatures while avoiding side product formation require noble metals such as Pt, Pd or Au, which leads to dramatic increases in cost⁴.

Chemical looping methane partial oxidation⁵ (CLPO) is an emerging approach that overcomes the above-mentioned shortcomings for syngas production. A CLPO process involves redox reactions taking place in two interconnected reactors: a reducer (or fuel reactor) and an oxidizer (also referred to as air reactor), shown in Figure 1(a). In contrast to conventional fossil fuel gasification and reforming processes, CLPO eliminates the need for an air separation unit, water–gas shift reactor, and acid gas removal unit. It has the potential to directly produce high-quality syngas with desirable H₂:CO ratios. The core of CLPO using natural gas as the feedstock involves complex redox reactions in which methane molecules adsorb and dissociate on metal oxide oxygen carrier surfaces. It also involves internal lattice oxygen ion diffusion in which

oxygen vacancy creation and annihilation occurs. These reactions can be engineered to withstand thousands of redox cycles⁵.

The recent progress in chemical looping technology for partial oxidation has advanced to the stage where successful pilot operation has been demonstrated and proven to be highly efficient with a minimal energy penalty in the process applications⁶. In this technology, the highest CO selectivity that the CLPO can reach is thermodynamically limited to 90% with accompanied 10% CO₂ generation. It is recognized that the CO₂ reduction in low purity syngas is extremely challenging and energy consuming, as CO₂ is among the most chemically stable carbon-based molecules⁷. This 10% of CO₂ in syngas can significantly reduce the productivity of value-added fuels or chemicals generated. Breaking away from the 90% CO selectivity limit to achieve a higher selectivity in redox reactions requires a different consideration from the metal oxide materials design and synthesis perspective. A promising approach is the use of metal oxide nanoparticles since the functionality of metal oxide materials intimately correlates with their structure in terms of size. Alalwan et al. investigated a set of unsupported α -Fe₂O₃ nanoparticles to explore the influence of particle size on CH₄ chemical looping combustion, and found decreasing the particle size from 350 to 3 nm increased the duration over which CH₄ was completely converted to CO₂. However, the unsupported nanoparticles underwent agglomeration and structural changes during the redox cycles, and as a result, they exhibited a steep decline in performance due to the loss of nanostructure.⁸

In the present work, we report a new approach to metal oxide oxygen carrier engineering for CLPO by designing and synthesizing nanoscale iron oxide carriers embedded in mesoporous silica SBA-15 (Fe₂O₃@SBA-15). Mesoporous silica is an engineered nanomaterial that has high surface area, ordered pore structures and high tunability of morphology. Its unique properties

have attracted broad attention in a number of applications such as environmental treatment, catalysis and biomedical engineering⁹⁻¹⁷. SBA-15 is a common mesoporous silica that has perpendicular nanochannels with a narrow pore size distribution which is suitable for nanoparticle separation and gas penetration. A schematic of our materials platform is outlined in Figure 1. We experimentally achieve a high CO selectivity >99%, which is by far the highest in CLPO systems. We also find that cyclic methane partial oxidation with nanoscale oxygen carrier materials can be performed with high selectivity at temperatures as low as 750 °C. These findings underscore the strong size-dependent effect of metal oxide oxygen carriers at the nanoscale on syngas selectivity and reactant conversion in redox processes. This work will have broader impacts not only on CLPO, but also on other chemical looping applications such as carbonaceous fuel conversion and utilization.

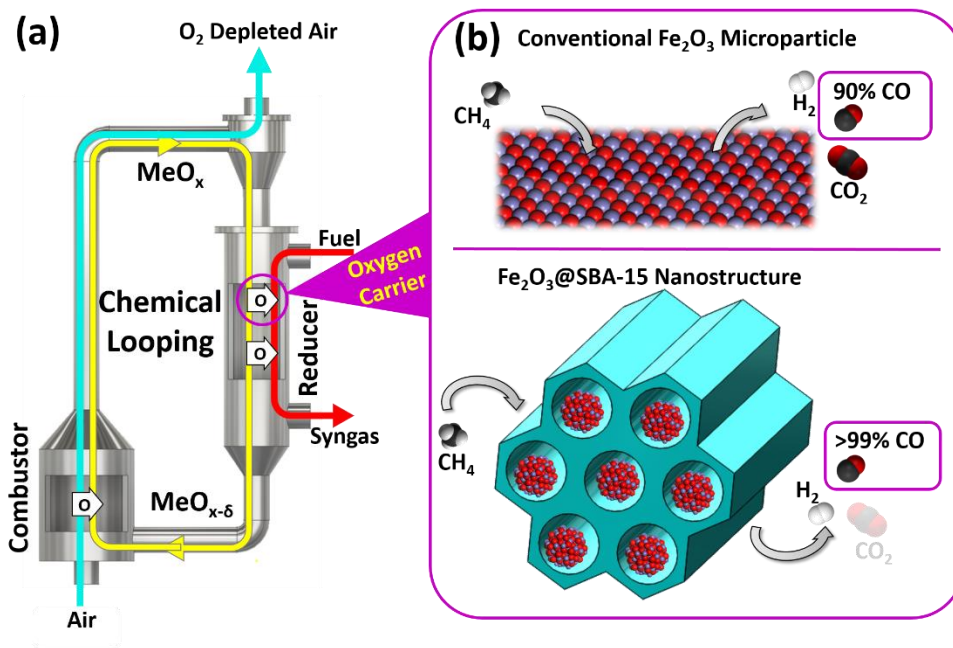


Figure 1 (a) Schematic of the chemical looping partial oxidation process, (b) structure and CO selectivity in conventional oxygen carrier vs Fe_2O_3 @SBA-15 oxygen carrier.

Results and Discussion

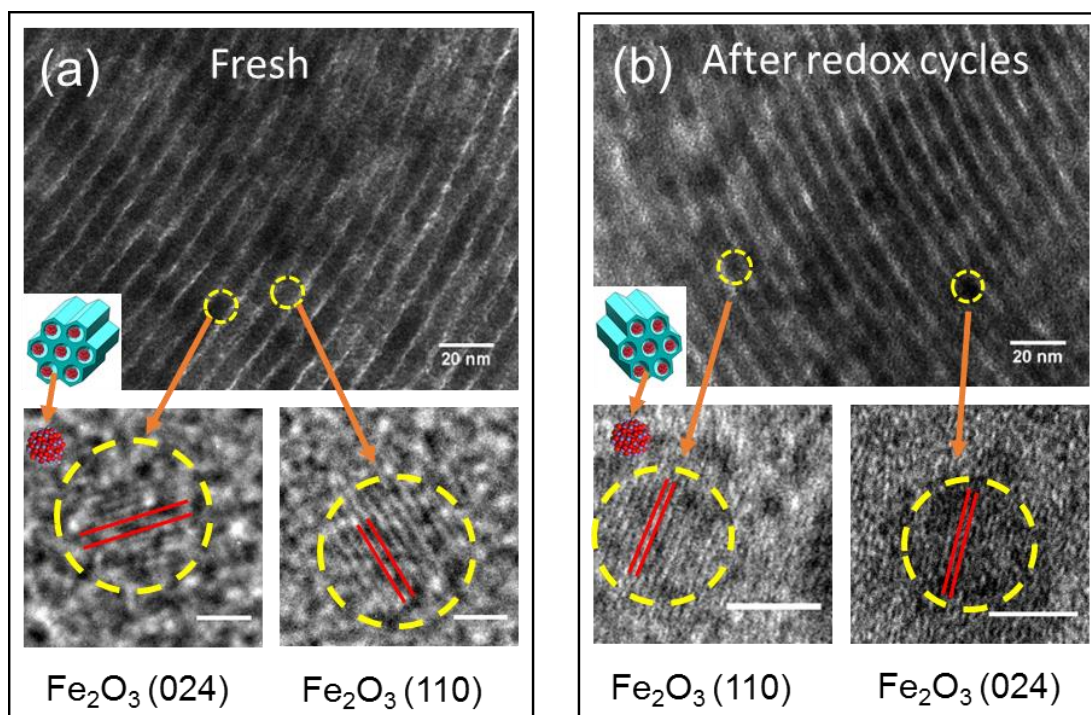


Figure 2. TEM images of (a) fresh Fe₂O₃@SBA-15 and HR-TEM images of two typical Fe₂O₃ nanoparticles (Scale bar represents 1nm); (b) Fe₂O₃@SBA-15 after multiple redox cycles and HR-TEM images of two typical Fe₂O₃ nanoparticles (Scale bar represents 5nm).

Figure 2 shows the TEM images of Fe₂O₃@SBA-15 before and after redox cycles. Nanoparticles with a size of 3-5 nm can be identified as α -Fe₂O₃ based on lattice fringes measurement in which $a = b = 5.038 \text{ \AA}$ and $c = 13.772 \text{ \AA}$. The images confirm that the nanoparticles remain embedded in SBA-15 nanochannels with identical morphology after multiple redox cycles. The particle size slightly increases to 5-8 nm after 75 redox cycles. This result indicates the high stability of Fe₂O₃@SBA-15 at high temperatures. The Fe₂O₃ particle size was also confirmed by N₂ physisorption and small angle X-ray diffraction (SAXRD), as shown in Supplementary Figure 1 and Supplementary Figure 2.

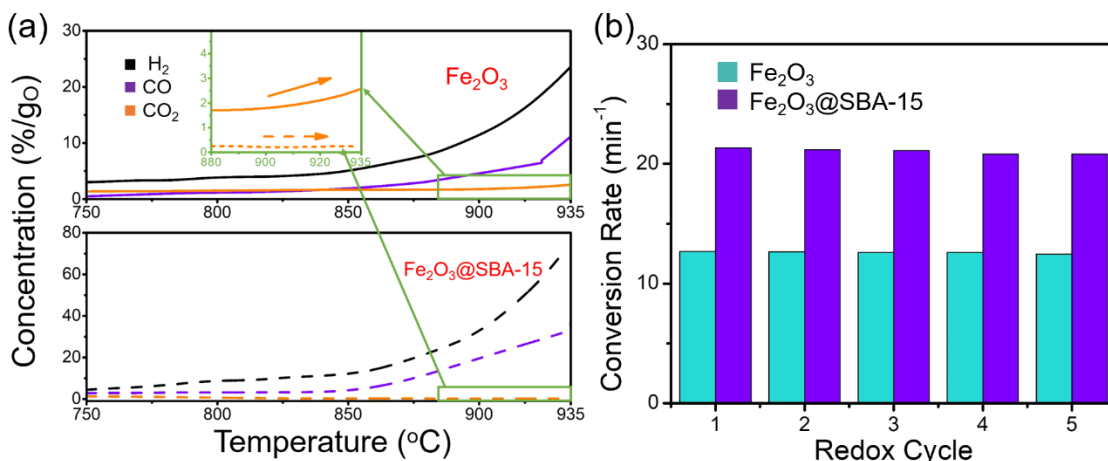


Figure 3. (a) Temperature ramped reduction results of Fe₂O₃@SBA-15 and Fe₂O₃; (b) Conversion rate during redox at 800°C

The reactivity and recyclability test results are shown in Figure 3. As shown in Figure 3a, a stable CO₂ concentration of <0.7%/g₀ is observed in Fe₂O₃@SBA-15 throughout methane partial oxidation, indicating a high syngas selectivity higher than 99.3%. In Fe₂O₃ without SBA-15 support, CO₂ formation is observed to increase with temperature, resulting in an average selectivity less than 87%. In the range of 750-935 °C, CO concentration from Fe₂O₃@SBA-15 is over 200% higher than Fe₂O₃ without SBA-15 support, suggesting a near 100% CO selectivity with significantly higher CO conversion rate.

Over 75 continuous redox cycles were carried out on both Fe₂O₃ samples with and without SBA-15 support. Five typical TGA redox cycles are shown in Figure 3b. The high recyclability is consistent with TEM observation. Fe₂O₃@SBA-15 not only has a high conversion rate, but is stable at high temperatures. This suggests that the separation of nanoparticles is essential in maintaining high CO selectivity, reactivity and recyclability. At 800°C, the conversion rate of Fe₂O₃@SBA-15 is 67% higher than Fe₂O₃ without SBA-15 support. The morphology of post redox nanoparticles can be found in Figure 2b, where Fe₂O₃@SBA-15

nanochannels remain almost identical to fresh samples. This demonstrates the high stability and anti-sintering effect of dispersed nanostructures at high temperatures.

To gain mechanistic insight into the role of the nanostructures in CO selectivity enhancement of Fe₂O₃@SBA-15, first-principles calculations were performed within the framework of density functional theory (DFT) using the Vienna Ab Initio Simulation Package (VASP)¹⁸⁻²⁰. Figure 4 shows calculated energies of CH₄ adsorption on Fe atop site and O atop site of (Fe₂O₃)_n nanoparticles as a function of n. The data of the previous computational study on CH₄ adsorption on Fe₂O₃ (001) surface are given by the filled circle. It can be seen that CH₄ adsorption energies dramatically decrease with increasing number, *n* when the sizes of Fe₂O₃ nanoparticles are at a relatively small scale. However, they decrease slowly with increasing *n* when the sizes are at relatively large scale. The strongest adsorption on (Fe₂O₃)₄ is CH₄ binding at the Fe atop site with an adsorption energy of 66.2 kJ/mol. The second stable configuration is CH₄ adsorption at the O atop site of (Fe₂O₃)₄ with an adsorption energy of 35.1 kJ/mol. When *n* increases from 4 to 60, the Fe atop adsorption becomes weaker with 43.9 kJ/mol lower adsorption energy. However, the adsorption at the Fe atop site and the O atop site of (Fe₂O₃)₆₀ nanoparticles is still stronger than adsorption on Fe₂O₃ (001) surface, as shown in Figure 5. This is because the average coordination number of surface Fe atoms in (Fe₂O₃)_n nanoparticle is smaller than that on Fe₂O₃ (001) surface. The undercoordination results in an upward shift of the Fe *d*-band, yielding high binding energies.

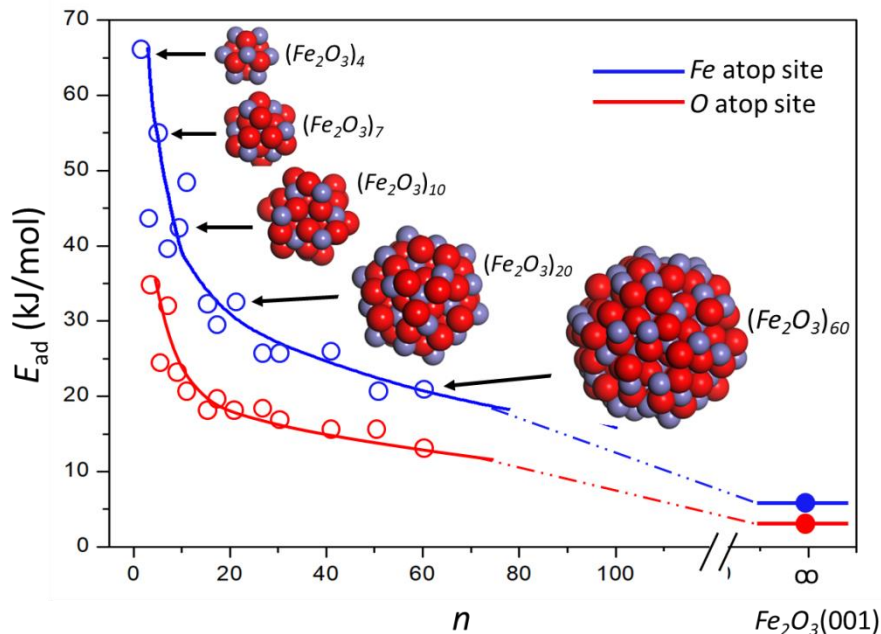


Figure 4. Calculated energies of CH_4 adsorption, E_{ad} (open circles, kJ/mol), on Fe atop site and O atop site of $(\text{Fe}_2\text{O}_3)_n$ nanoparticles as a function of n . The adsorption trends are shown by the solid blue and red lines.

After methane activation, C-H bonds are cleaved to generate a carbon atom and four hydrogen atoms. To determine the dominant pathway for converting the carbon atom to CO on $(\text{Fe}_2\text{O}_3)_n$, a relatively small nanoparticle $\text{Fe}_{40}\text{O}_{60}$ ($n=20$) was chosen as the model to calculate the reaction barriers. $\text{Fe}_{40}\text{O}_{60}$ has three chemically distinguishable types of lattice oxygen atoms: 2-fold coordinated lattice oxygen $\text{O}_{2\text{C}}$, 3-fold coordinated lattice oxygen $\text{O}_{3\text{C}}$, and 4-fold coordinated lattice oxygen O_{sub} . As such, there are three reaction pathways for CO formation as shown in Figure 5(a). The calculated barriers for $\text{CO}_{2\text{C}}$, $\text{CO}_{3\text{C}}$ and CO_{sub} formation are 37.2 kJ/mol, 69.6 kJ/mol and 58.5 kJ/mol, respectively. This result indicates C binding to $\text{O}_{2\text{C}}$ is the most favorable path, compared to C binding to $\text{O}_{3\text{C}}$ and O_{sub} because Fe-O bonds of low-coordinated lattice oxygen atoms are easier to break than high-coordinated lattice oxygen atoms. In contrast to $\text{Fe}_{40}\text{O}_{60}$, all lattice oxygen atoms in the topmost atomic layer of the Fe_2O_3 (001)

surface are three-coordinated atoms. Thus, the carbon atom on the Fe_2O_3 (001) surface converts to CO only via binding to O_{3c} , leading to a relatively high barrier of 61.2 kJ/mol as shown in Figure 5(b).

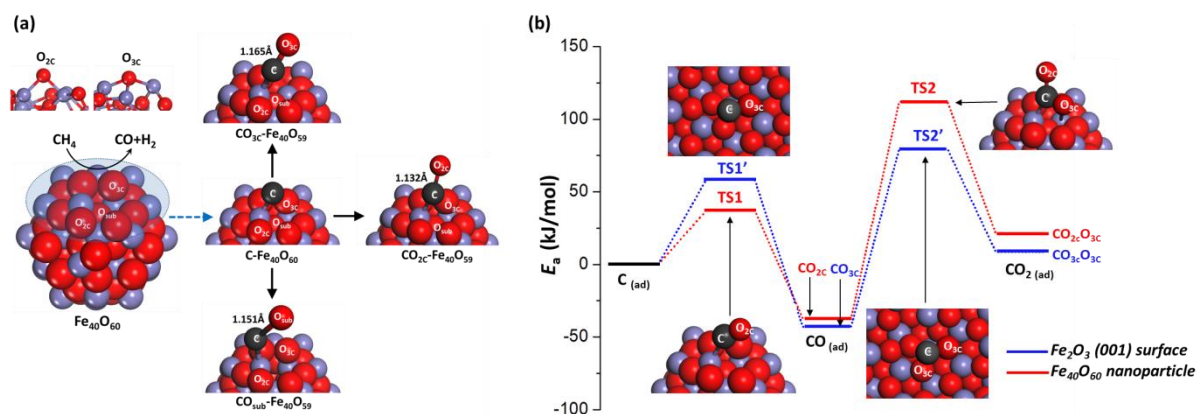


Figure 5. (a) Determining the pathway of CO formation on $\text{Fe}_{40}\text{O}_{60}$ nanoparticle. The C-O bond length and bond order are indicated. (b) Calculated barriers of CO and CO_2 formation on $\text{Fe}_{40}\text{O}_{60}$ ($n=20$) nanoparticles and Fe_2O_3 (001) surface.

The formed CO may further react with surface lattice O atoms to form CO_2 .^{21,22} For the $\text{Fe}_{40}\text{O}_{60}$ nanoparticle, the formation of CO_2 needs to overcome a barrier of 148.9 kJ/mol, which is 30.4 kJ/mol higher than that of CO_2 formation on Fe_2O_3 (001) surface. The high barrier with respect to CO_2 formation on $\text{Fe}_{40}\text{O}_{60}$ is attributed to the surface stress of nanoparticles, induced by surface atoms with unsaturated coordination. The surface stress leads to shorter and thus stronger Fe- O_{3c} bonds compared to Fe- O_{3c} bonds of the Fe_2O_3 (001) surface. The formation of CO_2 on $\text{Fe}_{40}\text{O}_{60}$ is endothermic, with the calculated reaction energy of 58.2 kJ/mol. These results indicate that the CO_2 formation on $\text{Fe}_{40}\text{O}_{60}$ is both kinetically and thermochemically unfavorable. Therefore, $\text{Fe}_{40}\text{O}_{60}$ nanoparticles significantly promote CO formation while inhibiting CO_2 production. Unfortunately, DFT-based calculations of large nanoparticles consisting of a few

thousand atoms, required for confirming this conclusion, are intractable to compute even on the most powerful supercomputers. Nevertheless, the experimental evidence for the extraordinary CO selectivity of Fe₂O₃ nanoparticles with the size of 5±3 nm indicates that nanostructuring makes Fe₂O₃ a more active oxide for CO production compared to bulk Fe₂O₃.

In summary, we demonstrate that Fe₂O₃ nanoparticles embedded in SBA-15 enables near 100% CO selectivity in chemical looping methane partial oxidation, which is so far the highest value in product selectivity observed for chemical looping systems. Moreover, the effective temperature for syngas generation is lowered to 750-935 °C, which is over 100 °C lower than current state-of-the-art processes. Nanostructured oxygen carriers are presented to exhibit little high-temperature reactivity property deterioration and adaptability to broader temperature operating windows for chemical looping operation conditions. These are important factors that can contribute to significant energy-saving reactor designs. The theoretical model and calculations reveal that the structure of the nanoparticles play a key role in CO selectivity enhancement of Fe₂O₃@SBA-15. The CH₄ adsorption energies and CO formation barriers depend not only on the nanoparticle size but also on the type of surface site exhibited by the nanoparticles. The small average coordination number of Fe atoms in the nanoparticle facilitates CH₄ adsorption and activation due to an upward shift of the Fe d-band, while the low-coordinated O atoms greatly promote Fe-O bond cleavage and CO formation, leading to a significant increase in CO selectivity. These findings contribute to a nanoscale understanding of the underlying metal oxide redox chemistry for chemical looping processes, and provide a systematic strategy toward the design of robust oxygen carrier nanoparticles with superior activity and selectivity.

Author Contributes

†Y.L., Q.L., and Z.C. contributed equally to this paper.

Competing Interests

The authors declare no competing interests.

References:

- 1 Luo, S., Zeng, L., Xu, D., Kathe, M., Chung, E., Deshpande, N., Qin, L., Majumder, A., Hsieh, T.-L., Tong, A., Sun, Z., & Fan, L.-S. Shale gas-to-syngas chemical looping process for stable shale gas conversion to high purity syngas with a H₂:CO ratio of 2:1. *Energy Environ. Sci.* **7**, 4104-4117 (2014).
- 2 Fan, L.-S., Zeng, L. & Luo, S. Chemical-looping technology platform. *AIChE J.* **61**, 2-22 (2015).
- 3 Qin, L., Guo, M., Liu, Y., Cheng, Z., Fan, J.A. & Fan, L.-S. Enhanced methane conversion in chemical looping partial oxidation systems using a copper doping modification. *Appl. Catal. B* **235**, 143-149 (2018).
- 4 Zeng, L., Cheng, Z., Fan, J.A., Fan, L.-S. & Gong, J. Metal oxide redox chemistry for chemical looping processes. *Nat Rev Chem.* **2**, 349–364 (2018).
- 5 Fan, L.-S. *Chemical Looping Partial Oxidation: Gasification, Reforming, and Chemical Syntheses*. (Cambridge University Press, 2017).
- 6 Chung, C., Qin, L., Shah, V. & Fan, L.-S. Chemically and physically robust, commercially-viable iron-based composite oxygen carriers sustainable over 3000 redox cycles at high temperatures for chemical looping applications. *Energy Environ. Sci.* **10**, 2318-2323 (2017).
- 7 Sun, Z., Ma, T., Tao, H., Fan, Q. & Han, B. Review: Fundamentals and challenges of electrochemical CO₂ reduction using two-dimensional materials. *Chem* **3**, 560-587 (2017).

- 8 Alalwan, H. A., Mason, S. E., Grassian, V. H. & Cwiertny, D. M. α -Fe₂O₃ Nanoparticles as Oxygen Carriers for Chemical Looping Combustion: An Integrated Materials Characterization Approach to Understanding Oxygen Carrier Performance, Reduction Mechanism, and Particle Size Effects. *Energy Fuels* **32**, 7959-7970 (2018).
- 9 Coleman, N. R., O'Sullivan, N., Ryan, K. M., Crowley, T. A., Morris, M. A., Spalding, T. R., Steytler, D. C., & Holmes, J. D. Synthesis and characterization of dimensionally ordered semiconductor nanowires within mesoporous silica. *J. Am. Chem. Soc.* **123**, 7010-7016 (2001).
- 10 Burke, A. M., Hanrahan, J. P., Healy, D. A., Sodeau, J. R., Holmes, J. D., & Morris, M. A. Large pore bi-functionalised mesoporous silica for metal ion pollution treatment. *J. Hazard. Mater.* **164**, 229-234 (2009).
- 11 Delaney, P., McManamon, C., Hanrahan, J. P., Copley, M. P., Holmes, J. D., & Morris, M. A. Development of chemically engineered porous metal oxides for phosphate removal. *J. Hazard. Mater.* **185**, 382-391 (2011).
- 12 Delaney, P., Healy, R. M., Hanrahan, J. P., Gibson, L. T., Wenger, J. C., Morris, M. A., & Holmes, J. D. Porous silica spheres as indoor air pollutant scavengers. *J. Environ. Monit.* **12**, 2244-2251 (2010).
- 13 Barreca, D., Copley, M. P., Graham, A. E., Holmes, J. D., Morris, M. A., Seraglia, R., Spalding, T. R., & Tondello, E. Methanolysis of styrene oxide catalysed by a highly efficient zirconium-doped mesoporous silica. *Appl. Catal., A* **304**, 14-20 (2006).
- 14 Ahern, R. J., Hanrahan, J. P., Tobin, J. M., Ryan, K. B., & Crean, A. M. Comparison of fenofibrates mesoporous silica drug-loading processes for enhanced drug delivery. *Eur. J. Pharm. Sci.* **50**, 400-409 (2013).
- 15 Abdallah, N. H., Schlumpberger, M., Gaffney, D. A., Hanrahan, J. P., Tobin, J. M., & Magner, E. Comparison of mesoporous silicate supports for the immobilisation and activity of cytochrome c and lipase. *J. Mol. Catal. B: Enzym.* **108**, 82-88 (2014).

- 16 Flynn, E. J., Keane, D. A., Tabari, P. M., & Morris, M. A. Pervaporation performance enhancement through the incorporation of mesoporous silica spheres into PVA membranes. *Sep. Purif. Technol.* **118**, 73-80 (2013).
- 17 Kumar, A., Madden, D. G., Lusi, M., Chen, K. J., Daniels, E. A., Curtin, T., Perry IV, J. J., & Zaworotko, M. J. Direct air capture of CO₂ by physisorbent materials. *Angew. Chem., Int. Ed.* **54**, 14372-14377 (2015).
- 18 Kresse, G. & Hafner, J. Ab initio molecular dynamics for liquid metals. *Phys. Rev. B* **47**, 558 (1993).
- 19 Kresse, G. & Furthmüller, J. Efficiency of ab-initio total energy calculations for metals and semiconductors using a plane-wave basis set. *Comput. Mater. Sci.* **6**, 15-50 (1996).
- 20 Kresse, G. & Furthmüller, J. Efficient iterative schemes for ab initio total-energy calculations using a plane-wave basis set. *Phys. Rev. B* **54**, 11169 (1996).
- 21 Cheng, Z., Qin, L., Guo, M., Xu, M., Fan, J.A. & Fan, L.-S. Oxygen vacancy promoted methane partial oxidation over iron oxide oxygen carrier in chemical looping process. *Phys. Chem. Chem. Phys.* **18**, 32418 - 32428 (2016).
- 22 Cheng, Z., Qin, L., Guo, M., Fan, J.A. & Fan, L.-S. Methane adsorption and dissociation on iron oxide oxygen carrier: role of oxygen vacancy. *Phys. Chem. Chem. Phys.* **18**, 16423-16435 (2016).